

Optimized Design of a Coupled-Inductor Buck Converter, 48 to 12 V, 1 kW, Using Planar Magnetics and GaN-FETs for MHz-Range Operation

Track 6. Vehicle Electrification-related Technologies

Abstract—The next generation of automotive vehicles and datacenters requires highly compact and efficient 48 V to 12 V point-of-load converters. This paper investigates the impact of coupling on the electrical properties of 2-phase buck converters operating in triangular current mode to achieve soft-switching. A novel planar inductor geometry with four poles and distributed air-gaps for operation beyond 1 MHz is presented that minimizes copper-losses from external proximity effect. An experimental prototype with 1 kW output achieves an impressive power density of 80 kW/l (1300 W/in³) and a peak efficiency of 96.3%, demonstrating the efficacy of the inductor structure.

Index Terms—coupled inductor, magnetic integration, planar inductor, triangular current mode

I. INTRODUCTION

With a growing power demand, power distribution in both conventional and electric vehicles presents an increasing challenge. Traditionally, 12 V are used to distribute the power to all auxiliary devices which requires large cable diameters. Moving to a 48 V distribution bus reduces the cost of the wire assembly and losses [1]. As most devices are still operating at 12 V, highly compact and efficient point-of-load converters are required. This conversion stage is a critical part of distributed power architectures and its performance has a direct impact on system-level efficiency, thermal design, and overall build volume.

With the rise of Gallium Nitride (GaN) power devices, operating converters in the MHz-range has become feasible, significantly reducing the size of the magnetic components [2]. At such high frequencies, hard-switched converters are inapt due to their large turn-on losses. Utilizing soft-switching, those losses are eliminated which allows operation in the MHz-range at excellent efficiencies [3]. Resonant converters inherently operate in soft-switching but are unsuitable when a regulated output voltage is required over a wide input voltage range. Traditional non-isolated converters such as buck or boost can also operate with soft-switching utilizing triangular current mode (TCM) as explained in the next section and only the small turn-on losses remain [4]. In soft-switched converters, magnetic components are often the main contributor to losses. Planar magnetics that use printed circuit board (PCB) windings are well-suited for those applications as they allow elaborate winding structures, effective cooling due to the large area per volume and direct integration with the other circuitry [5]–[8].

Lots of research was conducted for planar transformers but the design of compact and efficient planar inductors has its unique challenges due to the missing possibility for interleaving, the fringing of the air-gap and the DC-bias in the core. Utilizing multi-phase converters with coupled inductors is an effective way to reduce the volume and loss of the planar inductors as the flux can cancel out in certain areas [9].

In this paper, a 1 kW 2-phase coupled inductor buck converter for 48 to 12 V conversion is studied. To minimize the overall volume, a target switching-frequency range of 1 to 3 MHz was selected. Compared to previous work [5], [9]–[12], the low operating voltage requires a very low inductance whose design becomes particularly challenging due to the large phase current of 40 A and consequently over 80 A of ripple. Firstly, the effects of coupling on the electrical parameters are analyzed mathematically. Afterwards, different geometries for the single-turn inductor are optimized using a novel winding geometry and dual air-gaps. The most promising geometry based on the four-pole structure is implemented in an experimental prototype.

II. COUPLED INDUCTOR BUCK CONVERTER IN TCM

A. Working principle

The topology of the two phase coupled-inductor buck converter is shown in Figure 1. It operates like a conventional two-phase buck with both legs are switched 180° out of phase. When the leg 2 is pulled high, the current in leg 1 is also affected as shown in Figure 3: For positive coupling, the falling slope is steepened while for negative coupling it is flattened. The converter operates at very high ripple, more than twice the phase current such that the leg current becomes negative

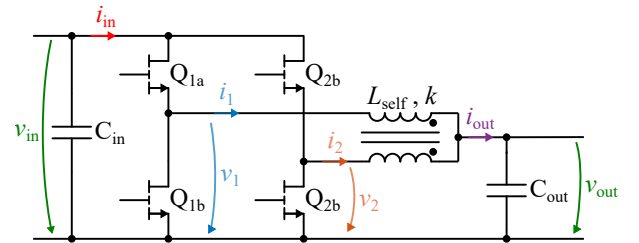


Fig. 1: Schematic of the Coupled Inductor Buck Converter.

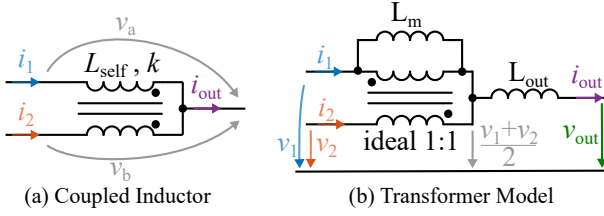


Fig. 2: The coupled inductor can be described with a self-inductance L_{self} and coupling factor k or by using an equivalent circuit consisting of an ideal 1:1 transformer with magnetizing inductance L_m and common output inductance L_{out} .

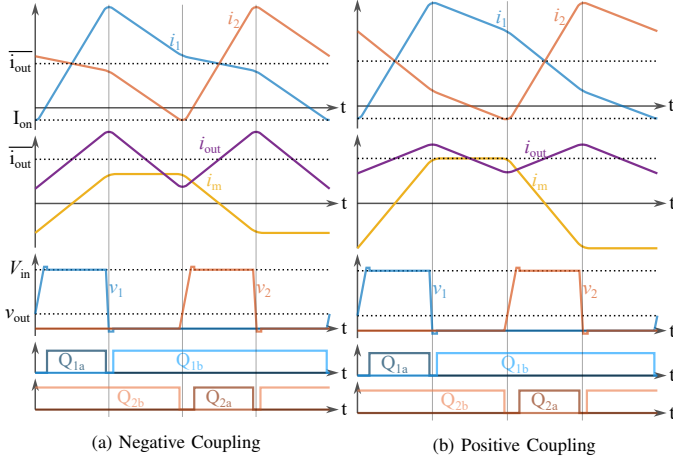


Fig. 3: Waveforms for positive and negative coupling. It can be seen that the slopes are changed but the behavior in the vicinity of the switching instances is fundamentally the same.

prior to the rising edge of each leg resulting in a zero voltage switching (ZVS) turn-on of all transistors. This mode is called TCM. Only the small turn-off losses are observed now [4].

B. Impact of the Coupling Factor

The symmetrical coupled inductor consists of two identical coils that are wound in a way, that the flux of one coil links with the flux of the second coil and vice versa with both coils connected on one side. This configuration can be described mathematically using

$$\begin{bmatrix} v_a \\ v_b \end{bmatrix} = \begin{bmatrix} 1 & k \\ k & 1 \end{bmatrix} L_{\text{self}} \begin{bmatrix} \frac{di_1}{dt} \\ \frac{di_2}{dt} \end{bmatrix} \quad (1)$$

with self-inductance L_{self} and coupling-factor k . Note that k can be positive or negative; the impact of that will be analyzed later. In order to simplify the equations and provide a more intuitive understanding, the equivalent circuit in Figure 2 is introduced. Both circuits are electrically equivalent for

$$\begin{aligned} L_{\text{out}} &= (1 + k) \frac{L_{\text{self}}}{2} \\ L_m &= (1 - k) \frac{L_{\text{self}}}{2}. \end{aligned} \quad (2)$$

The voltage at the virtual central node is now only dependent of the two leg voltages v_1 and v_2 decoupling the governing

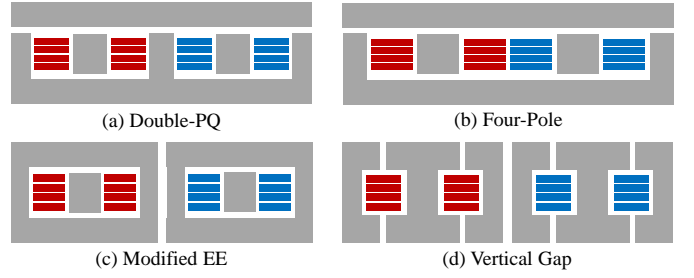


Fig. 4: Structure of the cores; Cut through the center, sie-view. First winding in red, second winding in blue.

equations:

$$\begin{aligned} \frac{di_{\text{out}}}{dt} &= \frac{1}{L_{\text{out}}} \left(\frac{v_1 + v_2}{2} - v_{\text{out}} \right) \\ \frac{di_m}{dt} &= \frac{1}{L_{\text{out}}} \left(\frac{v_1 - v_2}{2} \right) \end{aligned} \quad (3)$$

$$\text{with } i_{\text{out}} = i_1 + i_2 \text{ and } i_m = i_1 - i_2$$

From this, the differential equations for each interval can be easily calculated and equations for the important converter parameters can be derived. An effective dutycycle D_{eff} can be introduced with $D_{\text{eff}} = D$ for $D \leq 0.5$ and $D_{\text{eff}} = 1 - D$ for $D > 0.5$ to create universal equations. The peak-to-peak output ripple is then given by

$$\Delta I_{\text{out}} = \frac{2V_{\text{in}}}{f_s(1+k)L_{\text{self}}} D_{\text{eff}} \left(\frac{1}{2} - D_{\text{eff}} \right). \quad (4)$$

The peak-to-peak ripple in each leg which is important for soft-switching is

$$\Delta I_{\text{leg}} = \frac{V_{\text{in}} D_{\text{eff}}}{2f_s L_{\text{self}}} \left(\frac{2}{1+k} \left(\frac{1}{2} - D_{\text{eff}} \right) + \frac{1}{1-k} \right). \quad (5)$$

As mentioned before, for soft-switching I_{on} needs to be negative and generally needs to be below a certain value to guarantee a sufficiently short dead time which can be written as $\Delta I_{\text{leg}} \geq i_{\text{out}} + 2I_{\text{on,max}}$. This is fulfilled for

$$f_s < \frac{V_{\text{in}} D_{\text{eff}}}{2L_{\text{self}}(i_{\text{out}} + 2I_{\text{on,max}})} \left(\frac{2}{1+k} \left(\frac{1}{2} - D_{\text{eff}} \right) + \frac{1}{1-k} \right). \quad (6)$$

III. INDUCTOR DESIGN

A. Inductor geometry

Four different geometries, two coupled, and two uncoupled ones for reference, were considered for this application as shown in Figure 4. The Double-PQ structure was originally introduced by [5] and basically combines two EQ-cores placed next to each other. The four-pole structure is very similar but omits the central pole which creates separate paths for common-mode and differential-mode flux [9]. Both of these geometries were previously used with a two-piece core that only has air-gaps at the top. The dual air-gaps shown in Figure 4 are introduced in this work. The third geometry is basically an EE-Core but instead of one central gap, two gaps are used. Lastly, the vertical gap geometry proposed by

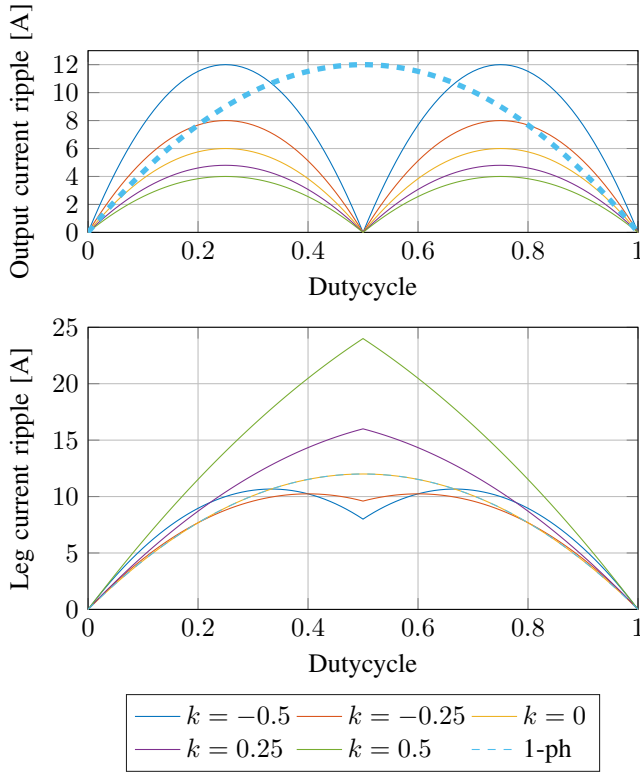


Fig. 5: Output current ripple and leg ripple for different coupling factors and constant input voltage. 1-ph for comparison. ToDo: Redo with normalized y-axis.

[7] is investigated which can partly compensate the internal proximity effect.

All designs use a single turn with all six layers in parallel which is very different from their original designs. Six layers were chosen due to the significantly cheaper manufacturing cost compared to higher layer counts. The inner layers have a thickness of $70\text{ }\mu\text{m}$ while the outer ones have only $35\text{ }\mu\text{m}$, due to the tight spacing of the selected gate-driver which required a $35\text{ }\mu\text{m}$ outer layer at the selected manufacturer to meet clearance constraints. Designs with more than one turn were not considered because the desired inductance and coupling-factor could not be achieved in that case due to fringing.

B. Material limitations

High-frequency ferrite materials for power applications have some unique properties that differ from those for lower frequency applications. TDK's PC200 was selected for this design as it exhibits very low loss in the range of 1 to 4 MHz. However, the performance of PC200 significantly degrades for a field strength $H_{\text{dc}} > 50\text{ A/m}$ and at $H_{\text{dc}} > 100\text{ A/m}$ its losses double¹ [13]. Therefore, the inductor was designed with a maximum H_{dc} of 40 A/m to have some margin.

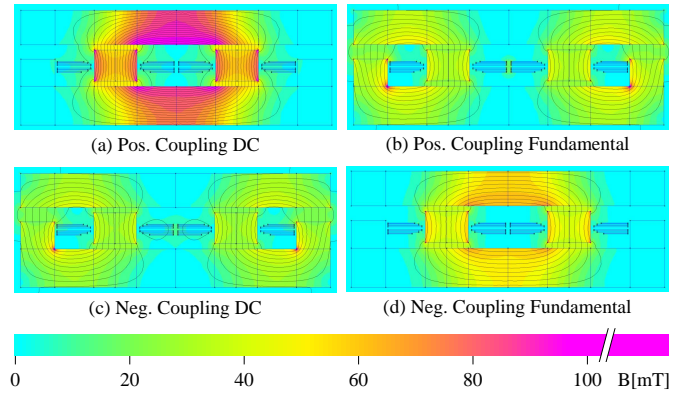


Fig. 6: Flux-Distribution for negative and positive coupling of otherwise identical designs for a DC phase current of 40 A and 100 A of ripple.

C. Positive vs negative coupling

Equation (4) and (5) are plotted in Figure 5 for positive and negative coupling-factors. While a strong positive coupling decreases ΔI_{out} it increases ΔI_{leg} . This is intuitive when looking at Equation (2): A positive coupling factor shifts inductance from the magnetizing to the output inductance, resulting in lower output current ripple but higher magnetizing current ripple. This means positive coupling require a larger L_{self} to achieve the same I_{on} if all other parameters remain the same.

Overall, positive coupling is slightly beneficial from an electrical point of view as it allows the usage of a larger L_{self} resulting in very low ΔI_{out} . However, in order to increase L_{self} , the air-gap has to be reduced, resulting in a higher flux-density and consequently higher core-losses or the number of windings has to be increased resulting in higher copper-loss. Furthermore, there is a very notable difference in the flux distribution as shown in Figure 6: For negative coupling, the two windings generate an opposing magnetomotive force at DC, resulting in a low flux and that circulates through the outer air-gaps. For positive coupling, the two magnetomotive forces are driving a DC-flux in the same direction causing a large flux that only circulates between the two windings where the reluctance is much lower. The peak flux-density is almost three times higher for positive coupling and as the core should be designed with respect to the H_{dc} limit, this means thicker top and bottom areas would be needed. Therefore, negative coupling is selected for this application². For the fundamental (and all other odd harmonics), the flux-paths are swapped compared to DC (and even harmonics) as shown in 6c) and d).

D. Simulation Process

For the simulation, the open-source 2D FEM software FEMM was used due to its high speed and easy integration

¹This effect is even more pronounced in NiZn materials which can be permanently damaged by large fields.

²Note that for lower frequency materials which are less affected by DC flux, the picture would change: Those designs would likely benefit from positive coupling as the flux-density at the fundamental is reduced.

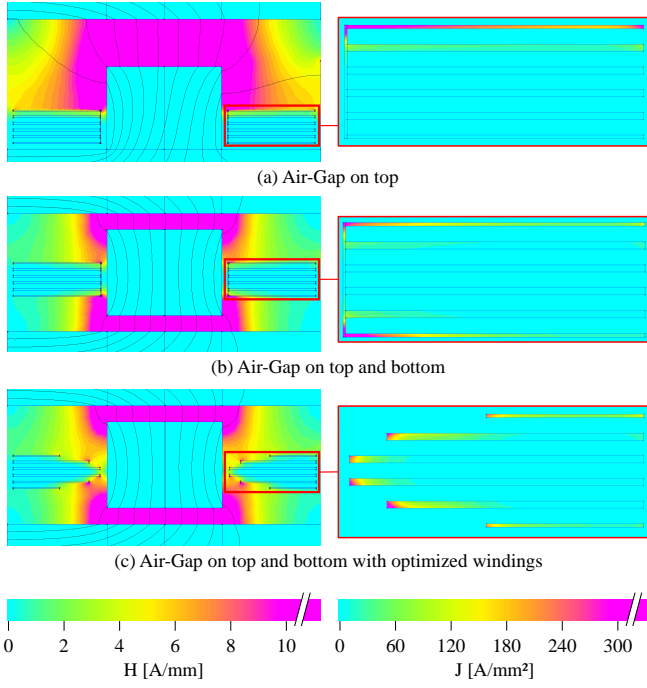


Fig. 7: Field and current distribution for different approaches. Because all layers are in parallel the current crowds in areas of large field-strength. By splitting the gap, the field gets distributed more evenly and the current distribution improves. Utilizing a smaller width for the outer layers, i.e. moving the copper away from the high-flux areas distributes the current even better.

TABLE I: Comparison of the size and loss of the optimized pillar and windings for the four-pole design.

	Volume [cm ³]	Copper Loss [W]
Original design	5.8	7.0
Air-Gap on top and bottom	5.5	5.7
Air-Gap on top and bottom, curved windings	5.3	5.0

with Matlab. As the core-structures are neither planar nor axisymmetric, the designs were first transformed to a planar structure. All cross-sectional areas are kept the same and the depth of the design is determined by the length of the winding³.

For validation, the design was also transformed into an axisymmetric structure (neglecting the effects of coupling). This has the advantage that the current distribution and consequently copper-loss is closer to reality at the expense of less-precise core-loss.

E. Split air-gap and optimized windings

The external proximity effect caused by the air-gap plays an important role for the current distribution and consequently the losses of this high-frequency inductor. The field-strength at the top of the windings is large and almost zero at the bottom. As a result, the AC current is only flowing in the top layers.

³As the current does not flow in the middle of the winding but closer to its center due to the shorter length and the magnetic field, the circumference taken not from the middle of the winding but closer to the inside

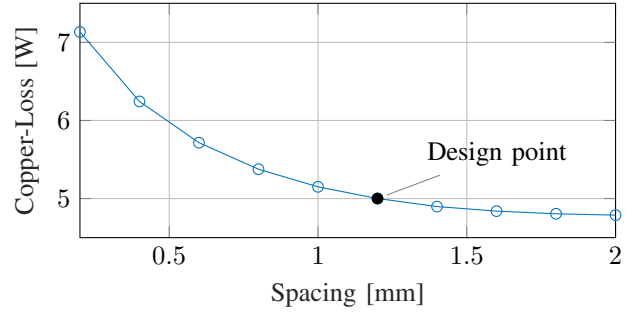


Fig. 8: Spacing between PCB and core vs. loss for the four-pole core (with curved windings and centered pillar). The distance between the PCB and the side air-gap core is fixed to 0.2 mm and the distance between PCB and bottom is varied. The pillar is always centered between top and bottom.

By centering the pillar vertically in the window such that there is an equal air-gap on the top and on the bottom, the field-strength is distributed much more uniformly and current flows in the top and bottom layers. This results in a 20 % reduction in losses, which can be reduced even further by using curved windings as shown in Table I.

F. Inductor Design Process

Using a brute-force algorithm was deemed impossible due to the many free variables with the custom design. Instead, a manual optimization was conducted for each structure. The desired switching-frequency was fixed to 1.5 MHz for full-load operation, the coupling-factor to -0.3, and the winding with to 3 mm as this showed a good balance between size and losses. The cross-sectional areas were designed to result in $H_{dc} \leq 40$ A/m and the air-gaps are defined by desired inductance (i.e. switching frequency) and coupling-factor. The spacing between PCB and top/bottom of the core is the only free variable and has to be chosen for a compromise between size and efficiency.

G. Vertical Air-Gap

The design with vertical air-gap showed a significantly lower loss compared to a traditional horizontal gap while having a much lower volume. This confirms the results from [7]. The main downside of this design is the significant external field on top and bottom of the inductor. This makes cooling difficult as no conductive material can be placed on top or bottom of the core, eliminating one of the typical advantages of planar inductors: The large area for cooling. Cooling from the side is proposed by [7] by having copper extending to the outside of the core where a heatsink can be attached but this is much less convenient and requires additional space.

H. Comparison of Core Structures

A comparison of the core structures is shown in Table II. All designs except the one with vertical gap use the optimized curved windings. The four-pole structure showed the lowest losses and volume.

TABLE II: Comparison of the size and loss of the different core structures for 1.5 MHz respecting the H_{dc} limit.

	Total Area [cm ²]	Height [cm]	Volume [cm ³]	Copper Loss [W]
Four-Pole	5.5	0.9	5.3	5.0
Double PQ	6.2	0.9	5.5	5.2
Vertical gap	8.0	0.7	5.8	5.6
UU core	8.1	1.1	8.9	6.0

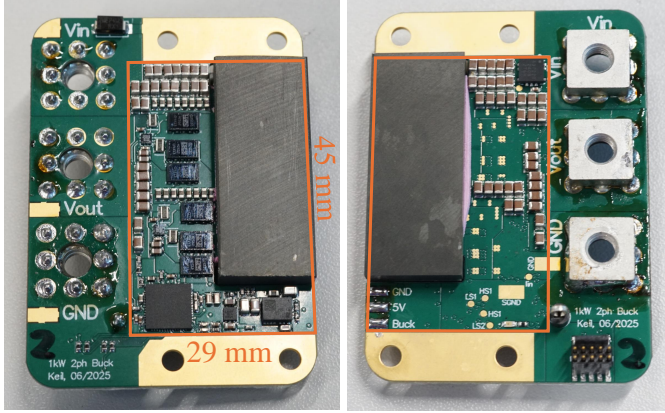


Fig. 9: Fully assembled prototype (without heatspreader). The converter area shown in orange is 45 x 29 x 9.5 mm. Outside of this area only the connectors for power and programming are placed as well as a protection diode and the programming resistors.

IV. EXPERIMENTAL PROTOTYPE

A. Hardware implementation

The assembled prototype is shown in Figure 9. The boxed volume of just 12.4 cm³ results in a power density of 80 kW/L (1300 W/in³). It uses Infineon's IGC025S08S1 80 V GaN HEMTs and Analog Devices' LT8418 gate drivers. Two parallel low side transistors per phase are used as the converter operates at a low duty cycle. To minimize the stray inductance, the decoupling capacitors for the half-bridges were connected to the devices with a vertical power-loop layout which uses the first inner layer as a return path as proposed by [14]. The whole system is controlled by a TI F280049C real-time microcontroller. Furthermore, the TPSM365R6 integrated buck-converter module is used for the housekeeping power-supply and an Allegro Microsystems ACS37220 monitors the input current. A total of 44 2.2 μ F 0805 100 V X7R capacitors are used to stabilize the input voltage resulting in a derated input capacitance of 20 μ F. This relatively small package was chosen because larger packages exhibit too much inductance causing resonance in the capacitor. At the output, 16 capacitors of the same type with a derated capacitance of 33 μ F are used to provide a low-ripple output voltage. Compared to other designs, this converter does not need any additional off-board capacitance.

B. Test results

The converter operates over the entire range as expected. The efficiency is shown in Figure 10 which reaches its max-

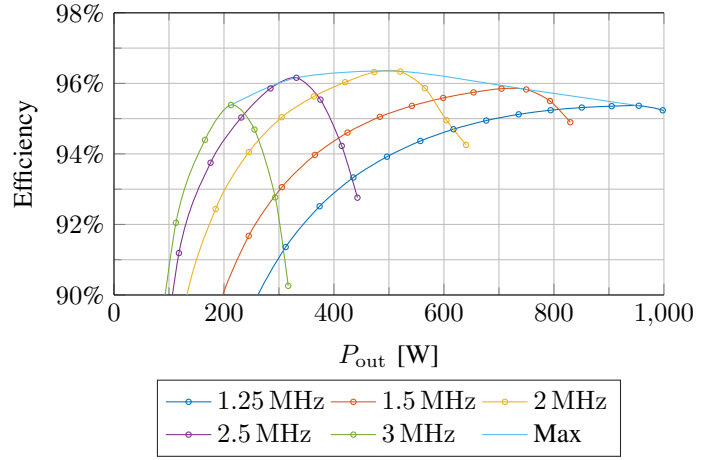


Fig. 10: Efficiency.

imum of 96.3% at around 550 W, demonstrating the efficacy of the inductor structure.

A more detailed analysis of the losses will be given in the final paper including a calculated contribution of the dielectric volume loss as introduced by [15].

REFERENCES

- [1] A. K. Kumawat and A. K. Thakur, "A Comprehensive Study of Automotive 48-Volt Technology," *International Journal of Mechanical Engineering*, vol. Volume 4, Jan. 2019, publisher: SSRG International Journal. [Online]. Available: <https://www.internationaljournalsrsg.org/IJME/paper-details?Id=73>
- [2] N. Weitz, S. Ehrlich, P. Freundl, J. Schültzke, and M. März, "A High Frequency Resonant Push-Pull Converter with a Single Integrated Magnetic Component," in *2023 IEEE Applied Power Electronics Conference and Exposition (APEC)*, Mar. 2023, pp. 435–440, iSSN: 2470-6647. [Online]. Available: <https://ieeexplore.ieee.org/document/10131366>
- [3] Y. Wang, O. Lucia, Z. Zhang, S. Gao, Y. Guan, and D. Xu, "A Review of High Frequency Power Converters and Related Technologies," *IEEE Open Journal of the Industrial Electronics Society*, vol. 1, pp. 247–260, 2020. [Online]. Available: <https://ieeexplore.ieee.org/document/9195796>
- [4] C. Marxgut, J. Biela, and J. W. Kolar, "Interleaved Triangular Current Mode (TCM) resonant transition, single phase PFC rectifier with high efficiency and high power density," in *The 2010 International Power Electronics Conference - ECCE ASIA*, Jun. 2010, pp. 1725–1732. [Online]. Available: <https://ieeexplore.ieee.org/document/5542048>
- [5] S. Wang, P. H. Pham, Q. Li, A. Nabih, and P. R. Prakash, "PCB Winding-Based Coupled Inductor for a High-Frequency DC/DC Converter with 99% Efficiency," in *2023 IEEE Applied Power Electronics Conference and Exposition (APEC)*, Mar. 2023, pp. 420–425, iSSN: 2470-6647. [Online]. Available: <https://ieeexplore.ieee.org/document/10131439>
- [6] B. Li, W. Qin, Y. Yang, Q. Li, F. C. Lee, and D. Liu, "A High Frequency High Efficiency GaN Based Bi-Directional 48V/12V Converter with PCB Coupled Inductor for Mild Hybrid Vehicle," in *2018 IEEE 6th Workshop on Wide Bandgap Power Devices and Applications (WiPDA)*, Oct. 2018, pp. 204–211. [Online]. Available: <https://ieeexplore.ieee.org/document/8569067>
- [7] J. Schäfer, D. Bortis, and J. W. Kolar, "Novel Highly Efficient/Compact Automotive PCB Winding Inductors Based on the Compensating Air-Gap Fringing Field Concept," *IEEE Transactions on Power Electronics*, vol. 35, no. 9, pp. 9617–9631, Sep. 2020, conference Name: IEEE Transactions on Power Electronics. [Online]. Available: <https://ieeexplore.ieee.org/document/8968357>
- [8] Y. Cai, M. H. Ahmed, Q. Li, and F. C. Lee, "Optimal Design of Megahertz LLC Converter for 48-V Bus Converter Application," *IEEE Journal of Emerging and Selected Topics in Power Electronics*, vol. 8, no. 1, pp. 495–505, Mar. 2020. [Online]. Available: <https://ieeexplore.ieee.org/document/8823928>

- [9] M. Hua, J. Chen, G. Xu, and H. Wu, "Ultra-thin Coupled Inductor for a GaN-Based CRM Buck Converter," in *2021 IEEE Workshop on Wide Bandgap Power Devices and Applications in Asia (WiPDA Asia)*, Aug. 2021, pp. 138–142. [Online]. Available: <https://ieeexplore.ieee.org/document/9656036/citations#citations>
- [10] C. Nan and R. Ayyanar, "A 1 MHz bi-directional soft-switching DC-DC converter with planar coupled inductor for dual voltage automotive systems," in *2016 IEEE Applied Power Electronics Conference and Exposition (APEC)*, Mar. 2016, pp. 432–439. [Online]. Available: <https://ieeexplore.ieee.org/abstract/document/7467908>
- [11] Y. Dong, "Investigation of Multiphase Coupled-Inductor Buck Converters in Point-of-Load Applications," Jul. 2009, publisher: Virginia Tech. [Online]. Available: <http://hdl.handle.net/10919/28469>
- [12] D. Sha, Y. Zhao, and D. Zhang, "ZVS-Interleaved Synchronous Buck DC-DC Converter With a Coupled Inductor by Varying Switching Frequency and Deadtime," *IEEE Transactions on Power Electronics*, vol. 37, no. 7, pp. 8190–8198, Jul. 2022, conference Name: IEEE Transactions on Power Electronics. [Online]. Available: <https://ieeexplore.ieee.org/abstract/document/9674799>
- [13] TDK, "High-Frequency, Low-Loss Ferrite Material PC200." [Online]. Available: https://product.tdk.com/de/techlibrary/productoverview/ferrite_pc200.html
- [14] D. Reusch and J. Strydom, "Understanding the Effect of PCB Layout on Circuit Performance in a High-Frequency Gallium-Nitride-Based Point of Load Converter," *IEEE Transactions on Power Electronics*, vol. 29, no. 4, pp. 2008–2015, Apr. 2014. [Online]. Available: <https://ieeexplore.ieee.org/document/6531683>
- [15] M. Baumann, C. Drexler, J. Pfeiffer, J. Schueltzke, E. Lorenz, and M. Schmidhuber, "Investigation of core-loss mechanisms in large-scale ferrite cores for high-frequency applications," in *2022 24th European Conference on Power Electronics and Applications (EPE'22 ECCE Europe)*, Sep. 2022, pp. 1–10. [Online]. Available: <https://ieeexplore.ieee.org/document/9907281>